PAPER • OPEN ACCESS

Laser pulse propagation and enhanced energy coupling to fast electrons in dense plasma gradients

To cite this article: R J Gray *et al* 2014 *New J. Phys.* **16** 113075

New Journal of Physics
The open access journal at the forefront of physics
Deutsche Physikalische Gesellschaft DPG | IOP Institute of Physics

Laser pulse propagation and enhanced energy coupling to fast electrons in dense plasma gradients

R J Gray[1], D C Carroll[1,2], X H Yuan[1,5], C M Brenner[1,2], M Burza[3], M Coury[1], K L Lancaster[2], X X Lin[4], Y T Li[4], D Neely[2,1], M N Quinn[1], O Tresca[1], C-G Wahlström[3] and P McKenna[1]

[1] Department of Physics, SUPA, University of Strathclyde, Glasgow G4 0NG, UK
[2] Central Laser Facility, STFC Rutherford Appleton Laboratory, Didcot, Oxfordshire OX11 0QX, UK
[3] Department of Physics, Lund University, PO Box 118, SE-22100 Lund, Sweden
[4] Beijing National Laboratory of Condensed Matter Physics, Institute of Physics, CAS, Beijing 100190, Peoples Republic of China
[5] State Key Laboratory of Transient Optics and Photonics, Xi'an Institute of Optics and Precision Mechanics, Chinese Academy of Sciences, Xi'an 710119, Peoples Republic of China
E-mail: paul.mckenna@strath.ac.uk

Received 5 June 2014, revised 8 October 2014
Accepted for publication 23 October 2014
Published 28 November 2014

New Journal of Physics **16** (2014) 113075
doi:10.1088/1367-2630/16/11/113075

Abstract

Laser energy absorption to fast electrons during the interaction of an ultra-intense (10^{20} W cm^{-2}), picosecond laser pulse with a solid is investigated, experimentally and numerically, as a function of the plasma density scale length at the irradiated surface. It is shown that there is an optimum density gradient for efficient energy coupling to electrons and that this arises due to strong self-focusing and channeling driving energy absorption over an extended length in the preformed plasma. At longer density gradients the laser filaments, resulting in significantly lower overall energy coupling. As the scale length is further increased, a transition to a second laser energy absorption process is observed experimentally via multiple diagnostics. The results demonstrate that it is possible to significantly enhance laser energy absorption and coupling to fast electrons by dynamically controlling the plasma density gradient.

Keywords: laser–plasma interaction, laser pulse propagation, fast electron generation

1. Introduction

Developments in intense short-pulse lasers have enabled new regimes of relativistic laser–plasma interactions to be explored and have led to new applications of high power lasers, such as the fast ignition approach to inertial confinement fusion (ICF) [1] and the production of ultra-bright pulses of high energy ions and radiation [2, 3]. Efficient absorption and transfer of laser energy to electrons is important for the development of these applications. The accelerated electrons transport energy, produce high energy radiation and drive the formation of electrostatic fields which accelerate ions. For example, a key challenge for the fast ignition approach to ICF is to couple sufficient energy (~20 kJ) from an ignition laser pulse via energetic ('fast') electrons to a hot spot in the compressed deuterium–tritium fuel. Maximizing the absorption of laser light into fast electrons is a key part of this challenge. Typical schemes involve the ignition laser pulse propagating through a coronal plasma with increasing density gradient to produce the fast electrons in the region of the critical density, n_c (the density at which the plasma becomes opaque to the laser light).

The various mechanisms by which laser energy is absorbed by electrons in the region of n_c are known to be sensitive to the plasma density scale length. These include the $j \times B$ [4], resonant absorption [5] and vacuum heating [6] processes, and can be broadly categorized as *surface* absorption mechanisms. In an extended underdense plasma, the laser pulse can undergo relativistic self-focusing [7, 8] and other propagation effects, including channel formation [9] resulting in energy coupling to electrons. These processes can be categorized as *volume* absorption processes [10]. Esirkepov *et al* [11], for example, provides an informative review of the effects of prepulse formation on the interaction of an intense laser pulse with a thin foil target in the context of optimizing ion acceleration. The variety of possible absorption mechanisms, coupled with the fact that the preformed plasma characteristics can vary greatly from experiment to experiment depending on the prepulse and amplified spontaneous emission (ASE) characteristics of the the drive laser pulse, means that significant challenges remain in terms of understanding and controlling fast electron generation in ultra-intense laser–solid interactions.

Experimentally, several studies have been performed to investigate the sensitivity of laser-to-fast electron energy coupling with the target density scale length. In separate investigations, large variations in $K\alpha$ production [12] and proton acceleration [13] are reported as a function of density scale length, and Culfa *et al* [14] report variations in the fast electron beam temperature. In addition, Scott *et al* [15] reports on energy coupling to fast electrons for three different density scale lengths, driven by changes in the laser ASE level, and from particle-in-cell (PIC) simulations infers the existence of two regimes of absorption in the case of large preformed plasmas. To build on this work and develop new understanding of the sensitivity of laser energy coupling and the resulting fast electron beam characteristics to the plasma density gradient, simultaneous measurements with multiple diagnostics of the energy transfer to fast electrons, as a function of a controlled and characterized density profile over a wide scale length range, are required.

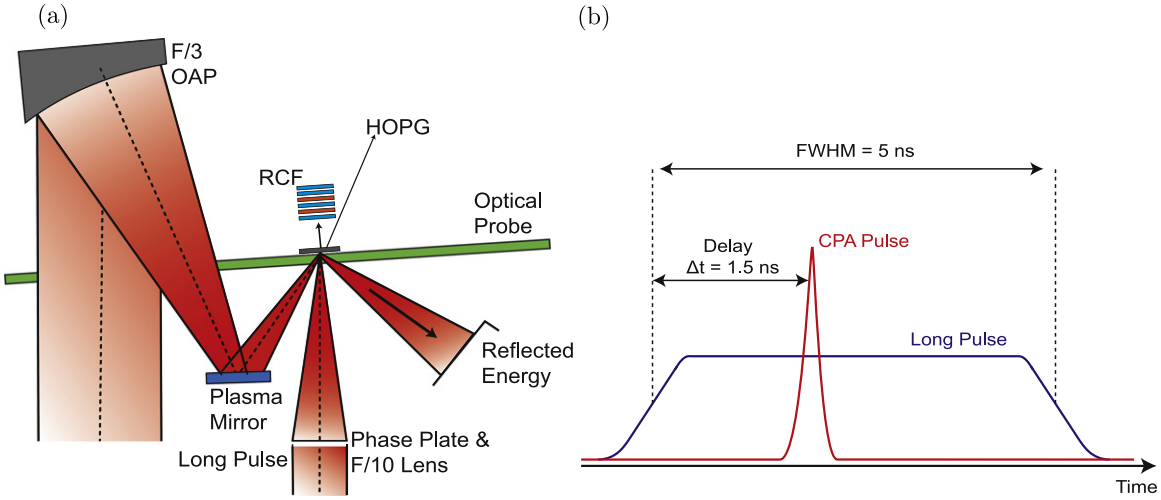

Figure 1. (a) Schematic diagram of the experiment arrangement. See main text for details. (b) Sketch illustrating the relative timing of the two laser pulses, which was fixed throughout the experiment—the leading edge of the long pulse arrives at the target 1.5 ns ahead of the short pulse. The plasma density scale length was controlled by variation of the intensity of the long pulse.

In this article, we demonstrate the importance of laser pulse propagation effects, including self-focusing, channelling and filamentation, and their sensitivity to plasma density gradients, on laser energy absorption and coupling to fast electrons at the front side of solids irradiated by ultraintense (10^{20} W cm^{-2}), picosecond laser pulses. Using a separate low intensity laser pulse to produce a controlled one-dimensional (1D) expansion, we measure strong variations (over one order of magnitude) in the coupling efficiency of laser energy to fast electrons, as diagnosed by the simultaneous measurement of laser energy reflection, x-ray emission and proton acceleration. The results demonstrate that it is possible to significantly enhance and control laser energy absorption and coupling to fast electrons by dynamically controlling the plasma density gradient, which is beneficial to the development of the aforementioned applications.

2. Experiment

The experiment was performed using the Vulcan laser at the Rutherford Appleton Laboratory. The laser delivered p-polarized pulses of 1054 nm light, focused using an *f*/3 off-axis parabola (OAP) onto the target at 19° with respect to target normal. The intensity contrast was measured to be $>10^{10}$ at 1 ns and $>10^{8}$ at 100 ps prior to the peak of the laser intensity [16]. A plasma mirror with a measured reflectivity of 67% was placed in the focusing beam, further reducing the intensity of the ASE pedestal by a factor of 50 [17, 18]. The laser pulse duration was 0.8 ps (full width at half maximum, FWHM), the on-target energy was 130 J and the focal spot diameter was 6.5 μm (FWHM), giving a calculated peak intensity, I_{SP}, equal to 1.2×10^{20} W cm^{-2}. Figure 1 shows an overview of the experiment arrangement.

A separate low intensity 5 ns-duration laser pulse (approximating a flat top intensity-temporal profile with a fast rise time of 0.2 ns) of 1054 nm wavelength light was used to produce a controlled expansion at the target front surface. This pulse was focused using an *f*/10 lens to a focal spot of 270 μm. A binary phase plate was used to produce a uniform intensity

Table 1. List of the long pulse, I_{LP}, and short pulse, I_{SP}, intensities used in the experiment and modelled in the simulations.

Case	I_{LP} (TW cm^{-2})	I_{SP} (10^{20} W cm^{-2})
A	0	1.2
B	2.1	1.2
C	3.5	1.4
D	5.5	1.3
E	18	1.4
F	23	1.2

distribution within the focal spot. This ensured an approximately 1D plasma expansion in the region of the ultra-intense laser pulse, which was centered on the focal spot of the lower intensity pulse. The scale length of the preplasma was varied by changing the energy of the long pulse, in the range 0 to 150 J, thereby changing its intensity, I_{LP}, and hence the plasma expansion velocity. The rising edge of the low intensity pulse arrived on target 1.5 ns ahead of the ultra-intense short pulse, as illustrated in the sketch in figure 1(b). The preplasma expansion was characterized using a frequency-doubled transverse optical probe [19].

The targets were layered planar foils consisting of a front layer of 40 μm aluminium, an 8 μm-thick copper layer for Cu–$K\alpha$ x-ray fluorescence and a rear layer of 75 μm CH to reduce the effects of fast electron refluxing on the measured Cu–$K\alpha$ signal [20].

Changes to the total laser energy absorption were characterized by measuring the laser light reflected from the target in the specular direction. A 12-bit CCD camera with imaging optics and filters was used to image the reflected 1ω laser light collected on a PTFE screen positioned in the specular reflection direction [21, 22]. To diagnose changes to the laser energy coupling to fast electrons, $K\alpha$ emission from the buried Cu layer and the energy spectrum and flux of protons accelerated by target normal sheath acceleration (TNSA) at the target rear surface were measured. The Cu–$K\alpha$ signal, which is produced by electrons above 8.98 keV, was measured using two highly ordered pyrolytic graphite (HOPG) crystal spectrometers, with Fujifilm imaging plate detectors. The sheath-field accelerating the protons to high energy is produced by the fast electrons which are transported through the target and emerge at the rear side. The spatial-intensity distribution of the resulting beam of multi-MeV protons was measured as a function of energy using passive stacks of dosimetry radiochromic film (RCF) [23], which were positioned 5 cm from the rear of the target and centred on the target normal axis. The Cu–Kα emission and proton acceleration were measured as a function of I_{LP} in the range 0–23 TW cm^{-2}. The cases explored are summarized in table 1.

The experimental results, presented in figure 2, show clear evidence of a transition between two different absorption regimes as the density scale length is varied. This is observed both in the measurements of the reflected laser light and in the measurements made to diagnose laser energy coupling to fast electrons. As shown in figure 2(a), the reflected laser energy is highest in the case of a sharp density gradient. As I_{LP} is increased to 5.5 TW cm^{-2}, the reflected light intensity decreases rapidly and then increases again, corresponding to an optimum condition for absorption for a preplasma driven by $\sim$2 TW cm^{-2} laser pulse. As I_{LP} is increased further, corresponding to increasing preplasma expansion and therefore scale length, the reflected energy slowly decreases again, indicating the onset of another absorption regime.

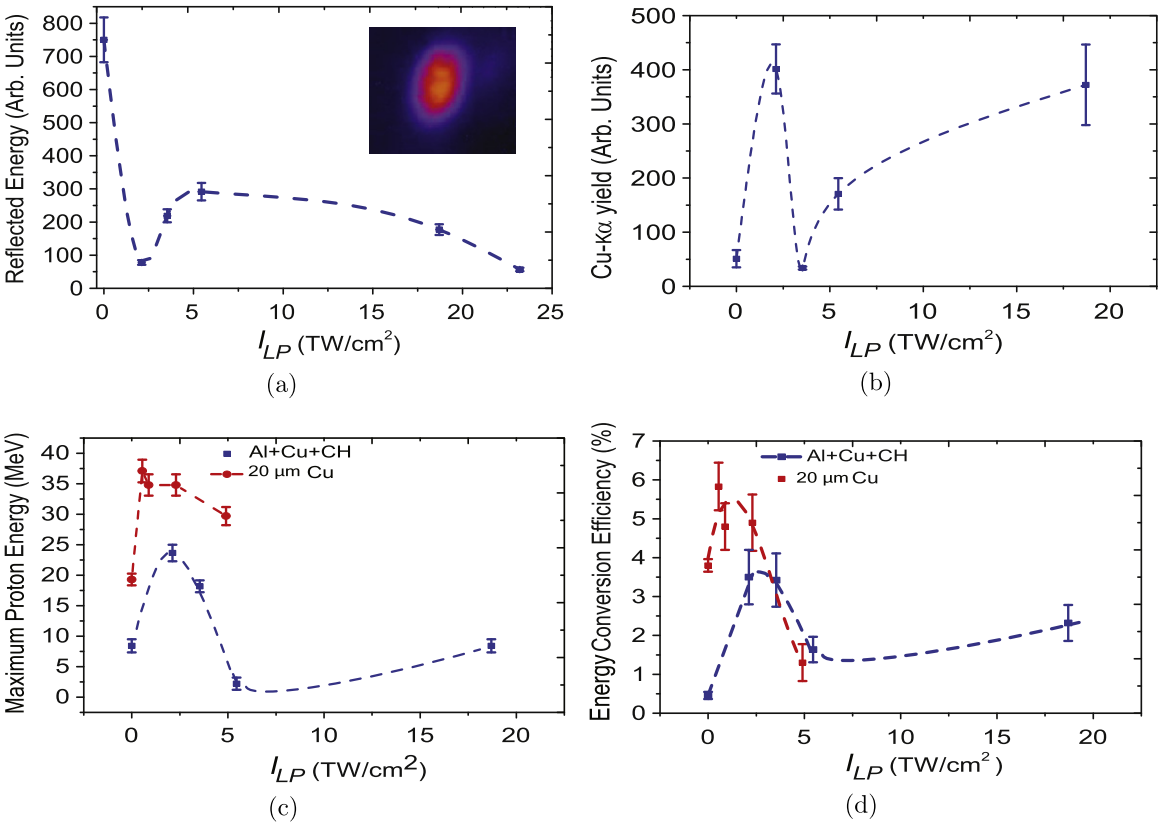

Figure 2. (a) Reflected laser energy as a function of I_{LP}. The inset shows an example image of the reflected laser beam as measured on the diagnostic screen. (b) Integrated Cu–Kα yield as a function of I_{LP}; (c) maximum proton energy, and (d) laser-to-proton energy conversion efficiency, as a function of I_{LP}. Results from [13] are reproduced for comparison. Note that the present results ('Al–Cu–CH') are obtained with a significantly thicker target (123 μm) than those of [13] ('20 μm Cu'), which results in an overall lower maximum proton energy and energy conversion efficiency.

As shown in figures 2(b)–(d), the Cu–Kα and proton acceleration measurements for the same laser shots as the data in figure 2(a) show a correlated behaviour in laser energy coupling to fast electrons, which in turn is correlated with the laser absorption. Clear enhancements of up to one order of magnitude are measured in the Cu–Kα yield and in both the maximum proton energy and laser-to-proton energy conversion efficiency at the same long pulse intensity of 2 TW cm^{-2}. The enhancement in maximum proton energy is in good agreement with a previous measurement made over a more limited range of long pulse intensities [13]. A further increase in the Cu–Kα emission is measured when increasing long pulse intensity to 18 TW cm^{-2}. There is a corresponding increase in the maximum proton energy and conversion efficiency, albeit that the latter increases are relatively small compared to the increase in Cu–Kα emission. Thus two clear regimes of laser energy absorption and coupling to fast electrons are observed. The first is very sensitive to the plasma density profile and is optimum for the preplasma driven by $I_{\mathrm{LP}} \sim 2$ TW cm^{-2} and the second slowly increases with increasing density scale length.

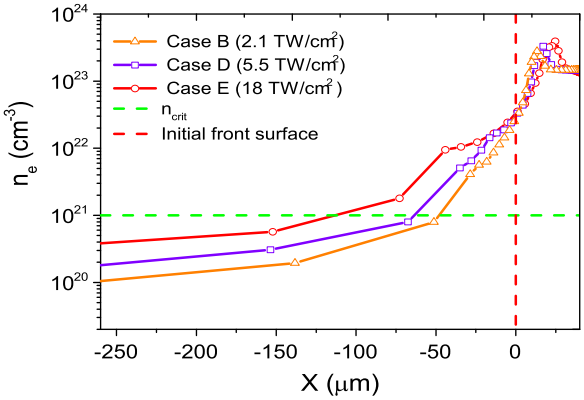

Figure 3. Electron density profiles at the front side of an Al target, as calculated using the HELIOS code, for three given long pulse intensities. The horizontal dashed line corresponds to the critical density and the vertical dashed line corresponds to the initial target surface position. Each profile is extracted at 1.5 ns.

3. Simulations

The highly sensitive nature of the laser energy absorption and coupling efficiency to fast electrons, particularly in the range I_{LP} = 0–5 TW cm^{-2}, points to significant changes in the absorption as a function of density scale length. To investigate this in more detail, we have performed two-dimensional (2D) PIC simulations of the laser pulse interaction with initial density gradients similar to those in the experiment, as defined using the output of radiation-hydrodynamic simulations.

Firstly, the plasma expansion at the front of the target was modelled for the parameters of the low intensity (long) pulse using the 1D Lagrangian radiation-hydrodynamic simulation code HELIOS [24]. In this approach, energy deposition is modelled assuming inverse bremsstrahlung for electron densities lower than the critical density and using a calculated absorption coefficient at the critical density surface. The material equation of state (EOS), in this case aluminium (as the front-surface irradiated material in the experiment), is included from the PROPACEOS EOS database. The initial temperature of the target is set as 0.1 eV. The simulations are run for 5 ns, with the axial density profile extracted at 1.5 ns, the time corresponding to the arrival of the CPA laser pulse in the experiment.

Figure 3 shows the calculated electron density profiles at the front surface of the target for three example values of I_{LP}: 2.1 TW cm^{-2}, 5.5 TW cm^{-2} and 18 TW cm^{-2} (cases B, D and E in table 1). The profile typically consists of a sharp decrease in density in the overdense region and a longer scale length underdense plasma stretching out towards vacuum. A fit was made to each calculated density profile and used to define the initial density conditions for PIC simulations of laser pulse propagation and energy absorption to electrons.

Next, the 2D EPOCH code was used to simulate the laser pulse propagation and energy transfer to fast electrons for the different preformed plasma profiles. The simulation box contained 21 000 × 7000 cells, extending over 150 μm × 50 μm. The maximum density in these simulations was 10n_c, which is sufficient considering that the pulse propagation and absorption physics investigated is occurring at densities lower than this. The simulated laser pulse was p-polarized, with duration equal to 800 fs and peak intensity equal to 1.2 ×10^{20} W cm^{-2} (to match

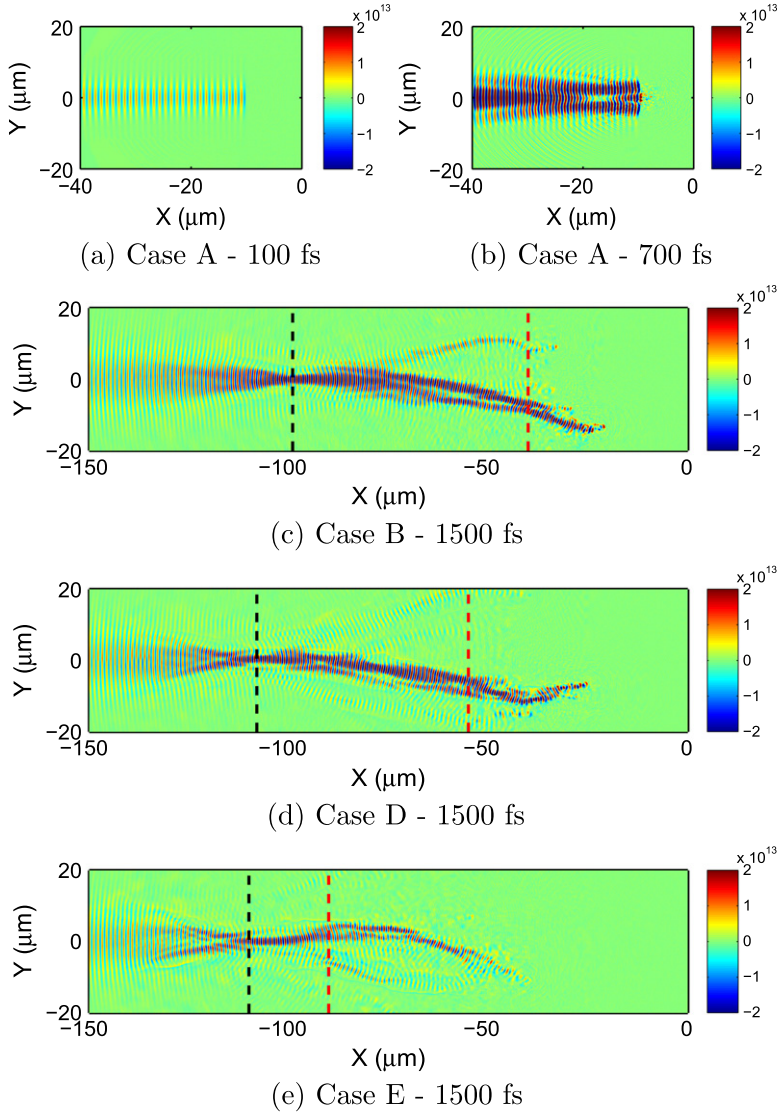

Figure 4. 2D PIC simulation results showing the laser electric field component E_y, in units of V m^{-1}: (a) case A, with front surface initially at −10 μm, after 100 fs; (b) case A after 700 fs; (c) case B after 1500 fs; (d) case D after 1500 fs; (e) case E after 1500 fs. The position $X = -10$ μm corresponds to the position of the $10n_c$ density in all cases. The red dashed line indicates the position of the n_c density and the black dashed line corresponds to the position of laser beam self-focusing.

the parameters of the CPA pulse in the experiment). In addition, a focusing laser geometry is used (approximating an *f*/3 laser cone) in order to accurately recreate the experimental spatio-temporal laser intensity profile over the entire simulation box.

2D maps of the laser *E*-field vector, the electron density and the cell-averaged electron kinetic energy (E_k) are shown in figures 4–6, respectively, for four example simulations: cases A, B, D and E as listed in table 1. Case A corresponds to a sharp density gradient. Cases B, D and E correspond to the density profiles for I_{LP} equal to 2.1 TW cm^{-2}, 5.5 TW cm^{-2} and 18 TW cm^{-2}, respectively. Because there is no extended preplasma in case A, a smaller simulation

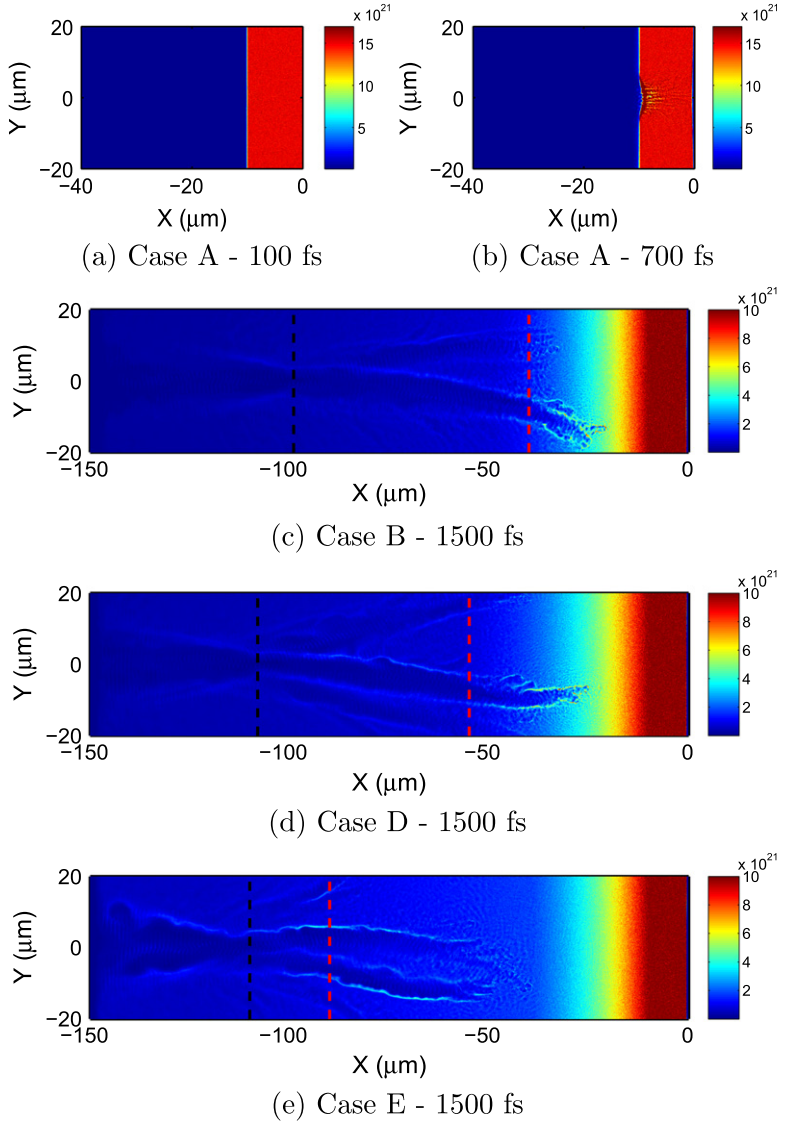

Figure 5. 2D PIC simulation results showing electron density, n_e in units of cm^{-3}. The caption is otherwise the same as for figure 4.

box (6000×7000 cells) was used to reduce computational requirements, but otherwise the cell size and other parameters are the same as for cases B, D and E. Furthermore, the simulation outputs for case A are shown at two example simulation times: (a) 100 fs, when the laser has just reached the target surface, and (b) 700 fs, when a significant fraction of the light has been reflected. The simulation outputs for cases B, D and E are all for a simulation time of 1500 fs, when the laser has propagated through the underdense part of the preformed plasma.

For case A the laser pulse propagates up to the sharp density transition at the target front surface, and drives a deformation (due to the ponderomotive force) and intrinsic rippling of the critical density surface [25], as shown in figure 5(b). The laser light is strongly reflected in this case and the incoming pulse is observed to be modulated by the reflected light. At later simulation times the deformed critical surface acts as a very short focal length parabolic mirror, as previously discussed by Schumacher *et al* [26]. The reflected laser light is thus

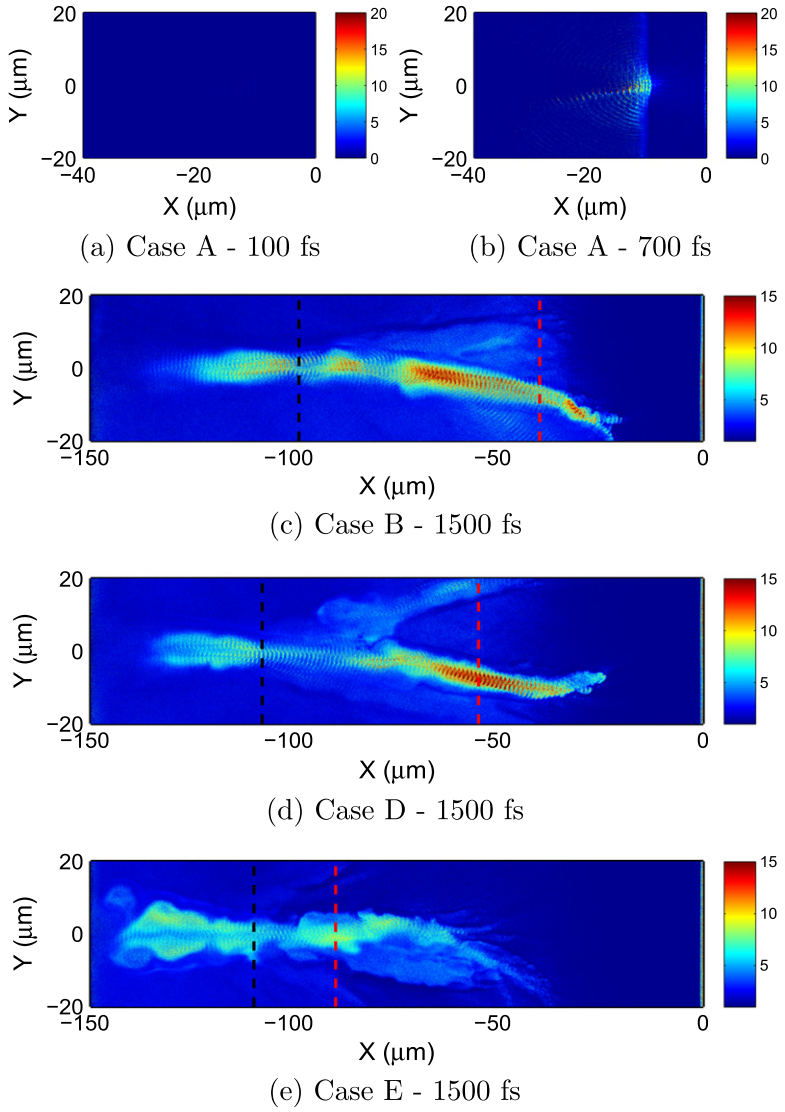

Figure 6. 2D PIC simulation results showing the cell-averaged fast electron kinetic energy, in units of MeV: the caption is otherwise the same as for figure 4.

focused and expands and interferes with the remainder of the incoming laser beam as shown in figure 4(b).

In contrast, in cases B, D and E, a number of laser pulse propagation effects are observed in the expanded underdense plasma. In all three cases the laser pulse self-focuses due to the combined effects of the ponderomotive force and relativistic nonlinearities. Self-focusing occurs due to the relativistic mass increase of plasma electrons and the expulsion of electrons from the propagation axis due to the transverse ponderomotive force of the laser pulse. The resulting density modulation increases the plasma refractive index on-axis, giving rise to a positive lensing effect [7, 8]. At relatively low densities of the order of $n_e < 0.1n_c$ (and laser pulse powers above the critical power for self-focusing [8]), the transverse ponderomotive force would be large enough to expel all electrons from the region of highest laser intensity,

generating an electron-free channel which guides the laser light. The length and stability of this channel depends on a number of factors, such as the rise time of the laser pulse and the growth of surface waves [27]. Due to computational limitations our PIC simulation box covers the high density range $0.1n_c \leqslant n_e \leqslant 10n_c$. At these higher densities a laser pulse undergoing relativistic self-focusing is subject to transverse instabilities, which lead to beam filamentation. This effectively competes with channel formation by splitting the beam into filaments [27]. As laser energy is coupled to the generation of fast electrons and light escapes from the filaments, the laser pulse power decreases and the propagation becomes susceptible to hosing-like behaviour which bends the laser away from the main propagation axis [28]. The growth rate of these instabilities are a function of the plasma frequency and thus the electron density. The fact that the density scale length is different in all three cases leads to different growth times of the filamentation and hosing instabilities along the axis of propagation. In case B the main filament propagates to a slightly higher density than case D (5×10^{21} cm^{-3} compared to 4×10^{21} cm^{-3}). In case E the highest density to which the laser pulse propagates is 1.6×10^{21} cm^{-3} and the beam is significantly more filamented than for B and D. Generally, with increasing density gradient the self-focusing moves closer to the critical density, which tends to increase the severity of the filamentation occurring.

It is instructive to examine the corresponding 2D maps of electron acceleration shown in figure 6. Two regions of laser energy coupling to fast electrons are observed. The dominant one is in the main filament as the laser propagates into the dense plasma in the vicinity of n_c (marked by the dashed red line). A second region of energy coupling to electrons occurs as the laser undergoes self-focusing (the focus position is marked by the dashed black line). In case B there is strong energy coupling in both regions, and generally along the length of the main filament, whereas in case D strong coupling occurs over a shorter length of the main filament in the vicinity of n_c. Case E clearly shows lower overall energy coupling. In this latter case the self-focusing effect is stronger than the other cases, which results from the higher density and thus larger change in refractive index across the beam when the electrons on-axis are expelled. The electron acceleration in the region of the self-focus is primarily occurring near the edge of the beam, where the electrons expelled from the centre pile up.

Measurements using a transverse optical probe for similar laser and target density profiles, as reported in McKenna *et al* [13], show experimental evidence of changes to the laser pulse propagation with increasing preplasma scale length. As shown in figure 7(a), for preplasma conditions similar to those in case B, a single long filament or channel is observed in the preformed plasma, whereas for conditions similar to case D (figure 7(b)), the propagating laser pulse has filamented. The former case corresponds to the peak of the laser energy coupling to fast electrons, whereas the latter results in significantly lower energy coupling, as shown in figure 2.

We next consider the energy spectrum of electrons accelerated into the target as extracted from the simulation results. This is sampled in the region of the critical density surface by extracting the cell-averaged electron density and kinetic energy at that position for each time step. The sample box is centred on the laser propagation axis, but intentionally limited to less than the full transverse extent of the simulation box in order to avoid the influence of any artificial edge effects. Figure 8(a) shows the time-integrated electron spectra for all four cases; A, B, D and E. The lower limit of the spectrum is set at $E_k > 2$ MeV to avoid the possibility of including numerically self-heated electrons.

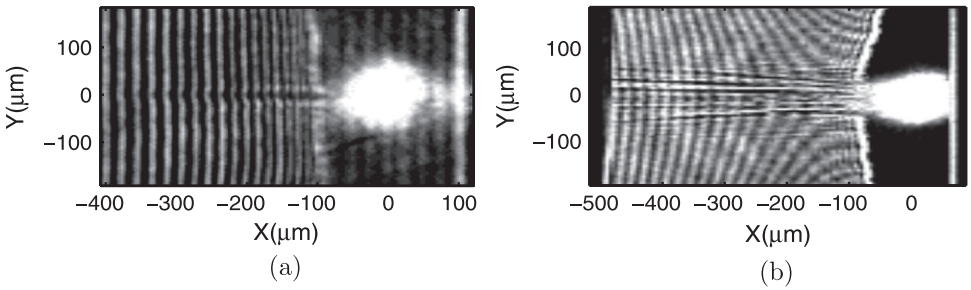

Figure 7. Optical interferometry measurements of the preplasma expansion and high intensity laser propagation at the target front side, from [13], for a plasma density profile similar to (a) case B, and (b) case D. A single extended filament or channel is formed in the first case, guiding the laser light to the critical surface. In the second case the propagating laser pulse is strongly filamented, which spreads the laser energy over a larger area in the plasma, resulting in a decrease in the laser intensity and therefore absorption.

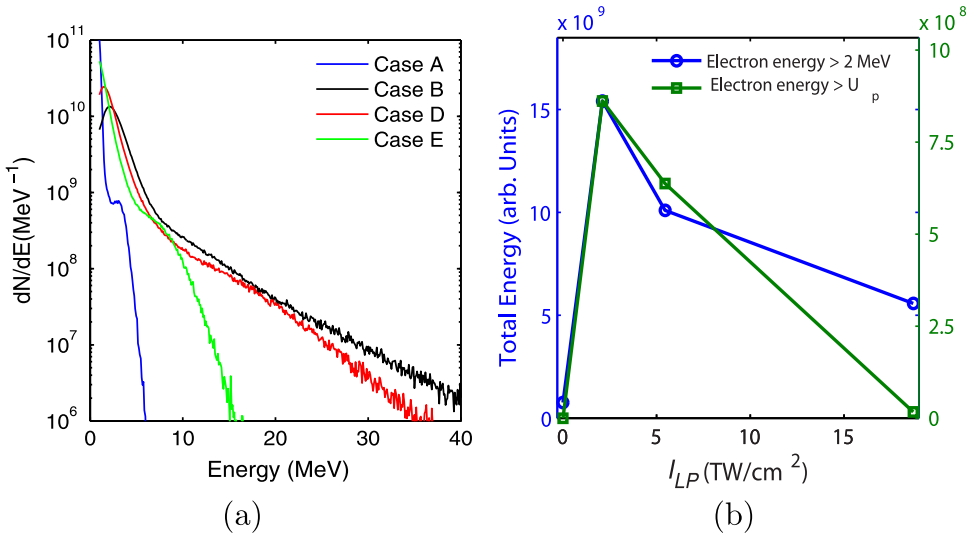

Figure 8. (a) Time integrated electron spectrum for $E_k > 2$ MeV at $X = -10$ μm in the simulation box for case A (blue) and at $X = -50$ μm for cases B (black), D (red) and E (green). The lower energy component of the electron spectrum is shown in the inset. (b) Integrated electron kinetic energy, for energies > 2 MeV in blue and for electrons energies $> U_p$, the ponderomotive potential, in green.

The spectra for cases B and D exhibit the highest electron energies and temperatures. An estimate of the laser-to-fast-electron energy conversion efficiency, both for the low energy and superthermal components of the spectrum, is obtained by integrating under the spectra, and plotted in figure 8(b). The overall optimum in the energy conversion at $I_{\mathrm{LP}} = 2.1$ TW cm^{-2} is in good agreement with the experiment data shown in figure 2. The measured secondary increase in energy coupling for longer scale length plasma, corresponding to $I_{\mathrm{LP}} = 18$ TW cm^{-2}, case E, is however not borne out in the simulation results.

4. Discussion

The following picture emerges from these experimental and simulation results. In the case of a sharp density gradient the laser pulse propagates unperturbed to the relativistically-corrected plasma critical density surface, converting laser energy to electrons by the aforementioned *surface* absorption processes. With an optimum preplasma density profile, the laser pulse undergoes gentle self-focusing and drives the formation of a plasma filament or channel, guiding the laser pulse and heating electrons over an extended length. As the density gradient is increased beyond an optimum, stronger self-focusing and filamentation of the laser occurs, significantly decreasing energy coupling to electrons.

Our experimental results indicate that laser energy absorption and coupling to fast electrons starts to increase again as the density scale length is further increased (as driven by $I_{\mathrm{LP}} \geqslant 18\ \mathrm{TW\,cm^{-2}}$). This is clearly observed both as a decrease in the reflected laser energy and as an increase in the Cu–$K\alpha$ emission. A corresponding, but smaller, increase in the maximum proton energy and conversion efficiency is also measured. Since the Cu–$K\alpha$ emission is more sensitive than TNSA-proton acceleration to fast electrons with energies in the tens of keV range (defined by the excitation energy of a K-shell transition), the secondary absorption process at high I_{LP} may predominately produce a colder spectrum of fast electrons. The fact that this additional energy coupling is not observed in the simulations suggests that this process is driven by other laser propagation effects.

Our simulation study focuses on laser pulse propagation over the density range $0.1n_{\mathrm{c}} \leqslant n_{\mathrm{e}} \leqslant 10n_{\mathrm{c}}$. At these near-critical densities, Pukov and Meyer-ter-Vehn [29] have shown, in 3D PIC simulations, that the generation of quasistatic magnetic fields about the axis of propagation can cause the unstable laser filaments to collapse into a single channel. The direct laser acceleration of electrons in a forward beam in high density plasma channels of this type has been measured experimentally [30]. High plasma densities over a sufficiently long propagation length are required to generate high enough magnetic fields sufficient for pinching the beam into a single channel and thus this effect may play a role in high density scale length plasmas. In addition, the long low density tail produced with such plasmas may lead to stable channel formation at $n_{\mathrm{e}} \leqslant 0.1n_{\mathrm{c}}$ due to complete electron evacuation on-axis, which could result in efficient laser energy coupling to electrons over longer distances [27]. Processes such as these may account for the measured second increase in absorption, but require a programme of simulations on a higher performance computer to investigate. This will be the subject of future work.

This study demonstrates that it is possible to significantly enhance laser energy absorption and coupling to fast electrons by controlling the front surface plasma density profile. As the processes responsible depend on the spatial- and temporal-intensity profiles of the laser pulse, there is significant scope for tuning both the laser pulse and target density profiles to maximize the energy transfer to fast electrons.

Acknowledgments

We acknowledge the expert support of the staff at the Central Laser Facility of the Rutherford Appleton Laboratory, the EPOCH PIC code development team and the use of the ARCHIE-WeST and ARCHER high performance computers. This work is supported by EPSRC (grant

numbers EP/J003832/1, EP/L001357/1 and EP/L000237/1-the UK Plasma HEC Consortium), by the Air Force Office of Scientific Research, Air Force Material Command, USAF (grant number FA8655-13-1-3008), the Swedish Research Council, the National Natural Science Foundation of China (grant numbers 10925421, 10720101075), and the National Basic Research Program of China (grant number 2007CB815101). Data associated with research published in this paper can be accessed by contacting the corresponding author.

References

[1] Tabak M *et al* 1994 *Phys. Plasmas* **1** 1626
[2] Daido H, Nishiuchi M and Pirozhkov A S 2012 *Rep. Prog. Phys.* **75** 056401
[3] Macchi A, Borghesi M and Passoni M 2013 *Rev. Mod. Phys.* **85** 751
[4] Kruer W L and Estabrook K 1985 *Phys. Fluids* **16** 430
[5] Ginzburg V L 1964 *Propagation of Electromagnetic Waves in Plasmas* (New York: Pergamon)
[6] Brunel F 1987 *Phys. Rev. Lett.* **59** 52
[7] Litvak A G 1969 *Sov. Phys.-JETP* **30** 344
[8] Max C, Arons J and Langdon A B 1974 *Phys. Rev. Lett.* **33** 209
[9] Najmudin Z, Krushelnick K, Tatarakis M *et al* 2003 *Phys. Plasmas* **10** 438
[10] Lefebvre E and Bonnaud G 1997 *Phys. Rev.* E **55** 1011
[11] Esirkepov T Zh *et al* 2014 *Nucl. Instrum. Methods* A **745** 150
[12] Lin X X *et al* 2010 *Phys. Rev.* E **82** 046401
[13] McKenna P, Carroll D C, Lundh O *et al* 2008 *Laser Part. Beams* **26** 591
[14] Culfa O *et al* 2014 *Phys. Plasmas* **21** 043106
[15] Scott R H H *et al* 2012 *Phys. Plasmas* **19** 053104
[16] Musgrave I *et al* 2010 *Appl. Opt.* **49** 6558
[17] Dromey B, Kar S, Zepf M and Foster P 2004 *Rev. Sci. Instrum.* **75** 645
[18] Ziener C *et al* 2002 *J. Appl. Phys.* **93** 768
[19] Benattar R, Popovics C and Sigel R 1979 *Rev. Sci. instrum.* **50** 1583
[20] Quinn M N *et al* 2011 *Plasma Phys. Control. Fusion* **53** 025007
[21] Streeter M J V *et al* 2011 *New J. Phys.* **13** 023041
[22] Pirozhkov A S, Choi I W, Sung J H *et al* 2009 *Appl. Phys. Lett.* **94** 241102
[23] Nürnberg F *et al* 2009 *Rev. Sci. Instrum.* **80** 033301
[24] MacFarlane J J, Golovkin I E and Woodruff P R 2006 *J. Quant. Spectrosc. Radiat. Transfer* **99** 181–90
[25] Wilks S C, Kruer W L, Tabak M and Langdon A B 1992 *Phys. Rev. Lett.* **69** 1383
[26] Schumacher D W, Kemp G E, Link A *et al* 2011 *Phys. Plasmas* **18** 013102
[27] Naseri N, Bochkarev S G and Rozmus W 2010 *Phys. Plasmas* **17** 033107
[28] Duda B J, Hemker R G, Tzeng K C and Mori W B 1999 *Phys. Rev. Lett.* **83** 197
[29] Pukhov A and Meyer-ter-Vehn J 1996 *Phys. Rev. Lett.* **76** 3975
[30] Gahn C, Tsakiris G D, Pukhov A *et al* 1999 *Phys. Rev. Lett.* **83** 1978